Journal of Power Sources 664 (2026) 238971

Contents lists available at ScienceDirect

Journal of Power Sources

journal homepage: www.elsevier.com/locate/jpowsour

Cycle performance and mechanism of Mg^{2+} storage in nanoflower-like 1T/2H-$MoSe_2$ cathode

Wei Yu [a], Yue Yang [a], Liuyu Song [b], Wenhao Zhou [a], Xi Chen [a], Lin zhu [c], Miao Xu [d,*], Fan Mo [a,**], Haibo Li [a,***]

[a] School of Resources and Civil Engineering, Northeastern University, Shenyang, 110819, China
[b] Baowu Group Xinjiang Bayi Iron and Steel Co., Ltd., Urumqi, 830000, China
[c] College of Sciences, Northeastern University, Shenyang, 110819, China
[d] Department of Science and Technology Development, Ministry of Natural Resources of the People's Republic of China, Beijing, 100000, China

HIGHLIGHTS

- 1T/2H-$MoSe_2$ was synthesized using a one-step solvothermal method.
- The cathode demonstrates high Mg^{2+} storage capacity and long cycle performance.
- Mg^{2+} forms a mixed covalent-ionic bond with the Se atoms at the interface.
- The heterophase junction interface reduces the $\triangle$E for Mg^{2+} intercalation.

ARTICLE INFO

Keywords:
$MoSe_2$
Heterophase junction
Cathode material
Long-cycle performance
Magnesium-ion storage of mechanism

ABSTRACT

Magnesium-ion batteries (MIBs) have emerged as a promising post-lithium energy storage technology due to inherent safety, low cost, high theoretical volumetric capacity and low redox potential. However, exploration of high-performance cathode materials, which can weaken electrostatic interactions and adapt to repeated Mg^{2+} insertion/extraction processes, remains a critical challenge. Herein, a facile one-step solvothermal synthesis method of $MoSe_2$ with heterophase junction structure (1T/2H-$MoSe_2$) is put forward. The enhancement of ion-covalent bonding between Mg^{2+} and surface Se atoms, and the reinforcement of interfacial electron coupling effect, induced by the heterophase junction are certified by density functional theory (DFT) calculation. Further reaction kinetics analysis shows that the electrochemical reaction in the cathode belongs to a capacitive process, while the anode side is controlled by diffusion and capacitive processes. This work highlights the crucial role of the heterophase junction in constructing high capacity and long-cycle Mg^{2+} storage materials.

1. Introduction

Magnesium-ion batteries (MIBs) have emerged as a transformative energy storage technology, leveraging the earth-abundant magnesium reserves, cost-effectiveness, and the high theoretical volumetric capacity of the Mg/Mg^{2+} redox couple with a low reduction potential [1]. However, the inherent challenges stem from the high charge density of Mg^{2+}, which induces strong Coulombic interactions with anion frameworks in cathode hosts, coupled with dynamic structural degradation mechanisms involving 15 % volumetric expansion and irreversible phase transitions during repeated Mg^{2+} (de)intercalation cycles [2].

Layered transition metal chalcogenides (TMCs) offer distinct advantages for multivalent ion storage systems, due to their van der Waals gap architectures, which enable precise structural engineering through interlayer spacing modulation [3]. It is crucial to note that the reduced Coulombic polarization between Se^{2-} and high-charge-density Mg^{2+} significantly lowers the desolvation energy barrier [3–5]. This, in turn, enables ultrafast Mg^{2+} intercalation kinetics with diffusion coefficients exceeding 10^8 cm^2 s^{-1} [6]. The remarkable stability of Mo-based TMCs is attributed to the near-degeneracy of Mo 4d and Se 4p orbitals, which

* Corresponding author.
** Corresponding author.
*** Corresponding author.
E-mail addresses: xumiaoee@163.com (M. Xu), mofan0118@163.com (F. Mo), lihaibo@mail.neu.edu.cn (H. Li).

https://doi.org/10.1016/j.jpowsour.2025.238971
Received 9 September 2025; Received in revised form 14 November 2025; Accepted 25 November 2025
Available online 27 November 2025

facilitates strong metal-chalcogen covalency via p/d-π* orbital hybridization. This electronic configuration effectively screens Mg^{2+}-host electrostatic interactions while maintaining structural integrity during deep cycling [7]. Emerging phase engineering strategies further enhance performance by constructing defects and metastable 1T/2H heterophase interfaces [8]. These interfaces simultaneously offer metallic-conductivity pathways and ion-storage-active 2H domains, thereby achieving an optimal balance between electronic/ionic transport and thermodynamic stability [9,10]. This critical breakthrough overcomes the traditional trade-off in multivalent battery electrodes. However, the mechanism of (de)intercalation of Mg^{2+} on 1T/2H $MoSe_2$ has not been reported yet.

Herein, Nanoflower-like 1T/2H $MoSe_2$ nanosheets were prepared by a one-step solvothermal method. The micromorphology, crystal structure evolution and surface chemical state distribution of the material were systematically analysed, and the properties in MIBs system were mainly tested and the long-cycling stability mechanism was explored. Further, we calculated and simulated the crucial parameters for comparison between 2H-$MoSe_2$-$Mg_{0.56}$ and 1T/2H-$MoSe_2$-$Mg_{4.22}$ in electrochemical processes via theoretical calculations, such as the charge density difference and Gibbs free energy gaps during magnesiation, evaluating the deposition sites of Mg^{2+}. This study provides a new insight for the design of heterophase junction cathodes for MIBs based on TMCs.

2. Experimental section

2.1. Synthesis of 1T/2H-$MoSe_2$ and the source of 2H-$MoSe_2$

$Na_2MoO_4 \bullet 2H_2O$ was utilised as the molybdenum source, while selenium powder was employed as the selenium source. Initially, 2 mg of selenium powder was added to 5 mL of N_2H_4, which was then stirred for a period of 4 h (solution A). Subsequently, 4 mM of $Na_2MoO_4 \bullet 2H_2O$ was dissolved in 20 mL of pure water and 10 mL of anhydrous ethanol (solution B). The two solutions should then be mixed and stirred for 2 h. Following this, the mixture should be subjected to a reaction at 180 °C for 20 h. The solid obtained by alternating washing and drying with deionized water and anhydrous ethanol is 1T/2H-$MoSe_2$. 2H-$MoSe_2$ is obtained by subjecting commercial molybdenum selenide, purchased from Macklin.

2.2. Materials characterization

The structural characterization was performed by X-ray diffraction (XRD, Rigaku SmartLab SE, Japan) using Cu Kα radiation ($\lambda = 1.5406$ Å) with a scanning range of 5–90° (2θ) and a scanning speed of 10°/min. Raman spectrum were collected on a confocal Raman spectrometer (Horiba Scientific LabRAM HR Evolution) with an excitation wavelength of 532 nm. The surface element composition, content, chemical valence states and chemical bonds of the samples were analysed by X-ray photoelectron spectroscopy (XPS, Thermo Scientific K-Alpha, USA). The morphologies of the samples were examined using field emission scanning electron microscope (SEM, Zeiss Merlin Compact, Germany) and transmission electron microscope (TEM, JEOL JEM-2100F, Japan).

2.3. Electrochemical characterization

The working electrode was prepared by mixing the 1T/2H-$MoSe_2$, carbon black, and polyvinylidene fluoride in N-methyl-2-pyrrolidone (NMP) solvent and pasting the slurry onto Cu foil, followed by drying under vacuum at 60 °C for 12 h. In addition, the coin cell was assembled with Mg foil polished with SiC sandpape as the anode, Alkylphenyl magnesium Chloride (APC) as the electrolyte, and glass fiber as the separator.

The charge/discharge measurements were tested at a potential range of 0.1–2.0 V using on a LANBTs-BT2018A electrochemical workstation at 298 K. Cyclic voltammetry (CV) were carried out on a LANLIKE-LK2010 battery tester at a scan rate of 0.1 mV s^{-1} with the voltage range of 0.1–2.0 V. Electrochemical impedance spectroscopy (EIS) measurements were performed on a LANLIKE-LK2010 battery tester in the frequency range of 10^6–10^{-2} Hz with an AC amplitude of 5 mV. The EIS data were fitted using the equivalent circuit model (R_s-(Rct//CPE)-W), where R_s is the solution resistance, Rct is the charge transfer resistance, CPE is the constant phase element, and W is the Warburg impedance.

2.4. Equations

The kinetic information about the electrochemical reactions is elucidated from b value according to the equation:

$$\log(i) = b\log(v) + \log(a) \quad \text{(S1)}$$

where i is the value of anodic and cathodic peak current, v is the value of scan rate, both a and b are constant. The b value is always used to tell apart the electrochemical reaction types. It is widely known the b value is in the 0.5–1.0 range. The electrochemical behavior is dominated by diffusion-controlled process, when the b value is draw near to 0.5; and capacitive process is the leading factor in electrochemical behavior, when the b value is close to 1.

The searching enquiry of the contribution of capacitance is made by the following equation:

$$i = k_1 v + k_2 v^{0.5} \quad \text{(S2)}$$

The $k_1 v$ in the above equation is due to the capacitive and the $k_2 v^{0.5}$ is down to diffusion-controlled.

2.5. Calculation of theoretical specific capacity

The theoretically specific capacity was calculated according to the following equation: C= (n*F)/M, in which n is the number of active sites for magnesium ions (calculated by DFT), F is the Faraday constant (26801 mAh mol^{-1}), and M is the relative molecular mass of active material. 1T/2H-$MoSe_2$: n = 38/9, M = 507.72, C = 222.85 mAh g^{-1}. 2H-$MoSe_2$: n = 5/9, M = 253.86, C = 58.65 mAh g^{-1}.

2.6. Density Functional Theory (DFT) calculation

Our study is performed using the Vienna ab initio simulation package (VASP) based on the density functional theory [11]. Based on the Perdew-Burke-Ernzerhof (PBE) function, the projected augmented wave method (PAW) and generalized gradient approximation (GGA) are implemented for the ion-electron interaction and exchange-correlation interaction functional [12,13]. The 21*21*1 gamma-centered denser k-points are used for the calculated geometry optimization and electronic structures of $MoSe_2$ unit-cells. Moreover, k points of 1*1*1 were adopted in the $MoSe_2$ supercell calculations. The periodic boundary conditions could be avoided by a 20 Å vacuum. A plane-wave cutoff energy 400 eV, maximum force $2*10^{-3}$ eV/Å (per atom), and energy convergence criterion 10^{-6} eV/atom are set to obtain accurate results. The van der Waals interactions are determined using the semi-empirical DFT-D3 approach [14].

3. Results and discussion

As illustrated in Fig. 1a, the prepared 1T/2H-$MoSe_2$ exhibited nanoflower morphology and was found to be highly agglomerated. In contrast, 2H-$MoSe_2$ displayed a thick layered stacking structure, as depicted in Fig. S1. EDX analysis manifested Mo and Se were uniformly distributed, with an atomic ratio of 1:1.85 (Fig. S2), which is roughly identical to the molecular formula. The advantages of porous structure and specific surface area can be intuitively observed in Fig. S3 [15]. The

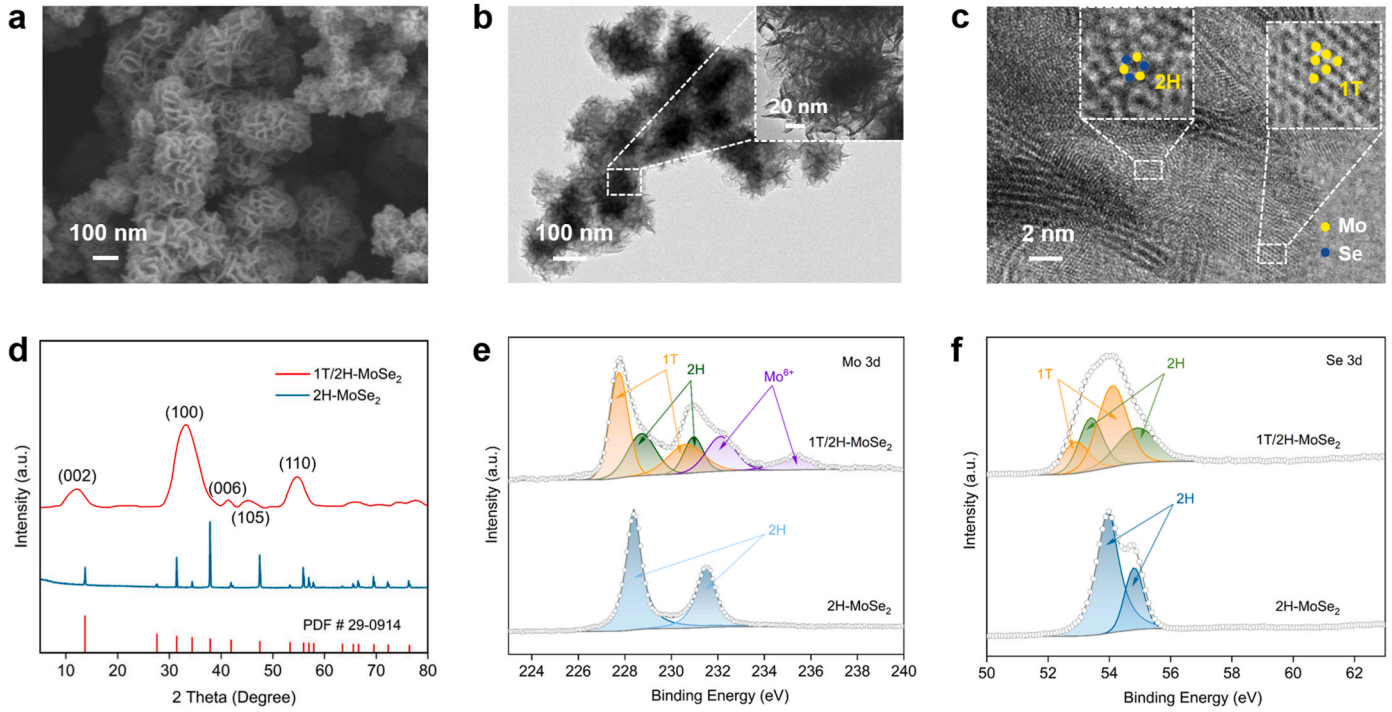

Fig. 1. a. SEM images of 1T/2H-$MoSe_2$. b. TEM and c. HRTEM images of 1T/2H-$MoSe_2$. d. XRD patterns of 1T/2H-$MoSe_2$ and 2H-$MoSe_2$. The high-resolution XPS spectra of e. Mo 3d and f. Se 3d for 1T/2H-$MoSe_2$ and 2H-$MoSe_2$, respectively.

microstructure of 1T/2H-$MoSe_2$ and 2H-$MoSe_2$ was further elucidated by TEM (Fig. 1b and S4b). The HRTEM images reveal the existence of two polymorphs and heterophase junction, with the exception of the 2H phase present in 2H-$MoSe_2$ (see Fig. 1c and Fig. S4c).

The present study explores the phases and chemical compositions of the sample thoroughly through XRD, Raman and XPS. The diffraction peaks at 12.6°, 33.6°, 41.7°, 45.3° and 54.8° of the XRD results shown in Fig. 1d agree well with the (002), (100), (006), (105) and (110) crystal planes of $MoSe_2$, respectively (PDF# 29–0914). The weak (002) plane and strong (100) plane are consistent with the 1T-$MoSe_2$. Furthermore, the (002) and (110) planes, which shift leftward relative to the standard card, indicate a transition from 2H to 1T in the sample [16]. In contrast to the case of 1T/2H-$MoSe_2$, the XRD consequence of 2H-$MoSe_2$ fully conforms to the standard card. This finding indicates that the 2H is the sole phase present in 2H-$MoSe_2$. This assertion is further substantiated by Raman spectroscopy. As demonstrated in Fig. S5, the peaks at 126, 161 and 199 cm^{-1} are attributed to the J_1, J_2 and J_{3g} modes of 1T-$MoSe_2$, while the two peaks at 225 and 282 cm^{-1} correspond to the A_{1g} and E^1_{2g} modes of 2H-$MoSe_2$. The above analysis results are consistent with the TEM characterization, which proves the coexistence of 1T-$MoSe_2$ and 2H-$MoSe_2$.

As illustrated in Fig. 1e, the Mo 3d spectrum of the prepared material is displayed. The Mo 3d spectrum of 1T/2H-$MoSe_2$ has been deconvoluted into three doublet peaks. The peaks at 228.9 eV (Mo $3d_{5/2}$) and 231.8 eV (Mo $3d_{3/2}$) are ascribed to 1T-$MoSe_2$, and the peaks at 229.6 eV (Mo $3d_{5/2}$) and 232.1 eV (Mo $3d_{3/2}$) are ascribed to 2H-$MoSe_2$ [17,18]. Evidently, the energies of 233.1 eV and 236.6 eV are attributable to Mo^{6+}, which can be ascribed to the incomplete selenization process [19,20]. Furthermore, the multivalent states of Mo have been demonstrated to facilitate ion diffusion [21]. The 1T/2H phase ratio in $MoSe_2$ can be quantitatively determined via XPS, with consistent verification by Raman spectroscopy and HRTEM. In this study, the phase ratio of 1T/2H-$MoSe_2$ was quantified by integrating the peak areas of Mo 3d spectra [22,23]. The results indicate that the content of the 1T phase is 44 %, while that of the 2H phase is 56 %. This calculation was derived from the $3d_{5/2}$ peaks of 1T-$MoSe_2$ (228.9 eV) and 2H-$MoSe_2$ (229.6 eV).

A previous study demonstrated that N_2H_4 functions as a dual agent, promoting the formation of the 1T phase. During the solvothermal process, the material undergoes decomposition, yielding N-containing components that function as electron donors. These components are embedded within the layers of $MoSe_2$ and facilitate the transfer of electrons to the Mo 4d orbitals. This electron injection results in the 4d orbitals of the 1T phase becoming half-filled, thereby enhancing its thermodynamic stability. This configuration exhibits reduced stability in comparison to the 2H phase. The increase in N_2H_4 content results in an increase in the nitrogen components of $MoSe_2$, which consequently leads to an enhancement in the proportion of the 1T phase [23]. However, the Mo 3d spectrum of 2H-$MoSe_2$ is deconvoluted into a couple of doublet peaks. The results of the Se 3d spectra (Fig. 1f) are consistent with those of the Mo 3d spectra, indicating that both the phase of 1T and 2H have been prepared successfully.

The electrochemical magnesium storage performance of 1T/2H-$MoSe_2$ was measured in the range of 0.1–2.0 V and compared with 2H-$MoSe_2$ (Fig. 2). It was observed that there was a slight negative migration of redox peaks in the second and third cycles compared to the first cycle (Fig. 2a and Fig. S6a). This suggests that a surface activation process occurred for 1T/2H-$MoSe_2$ at the beginning of the cycling process [24,25]. The continuous increase in the area under the curve (AUC) of the CV curve further confirms the occurrence of an activation reaction. The CV curves of 1T/2H-$MoSe_2$ exhibit two pairs of redox peaks at approximately 1.77/1.91 and 0.82/1.22 V, which can be ascribed to a multistep magnesium ion insertion.

The larger area of CV curve indicates that 1T/2H-$MoSe_2$ possesses superior magnesium storage capacity. The discharge-charge plots of 1T/2H-$MoSe_2$ and 2H-$MoSe_2$ at 50 mA g^{-1} are presented in Fig. S6b and Fig. S6c, and are consistent with the CV curves. The cycle performance of 1T/2H-$MoSe_2$ and 2H-$MoSe_2$ at 50 mA g^{-1} is presented in Fig. 2b. The coulombic efficiency of the initial cycle is merely 31 %, which originates from multiple synergistic factors causing irreversible capacity loss, among which the dynamic evolution of the solid electrolyte interphase (SEI) at the Mg anode/electrolyte interface (2 PhMgCl and $AlCl_3$ in THF) is the dominant factor [26–29]. According to recent systematic studies of

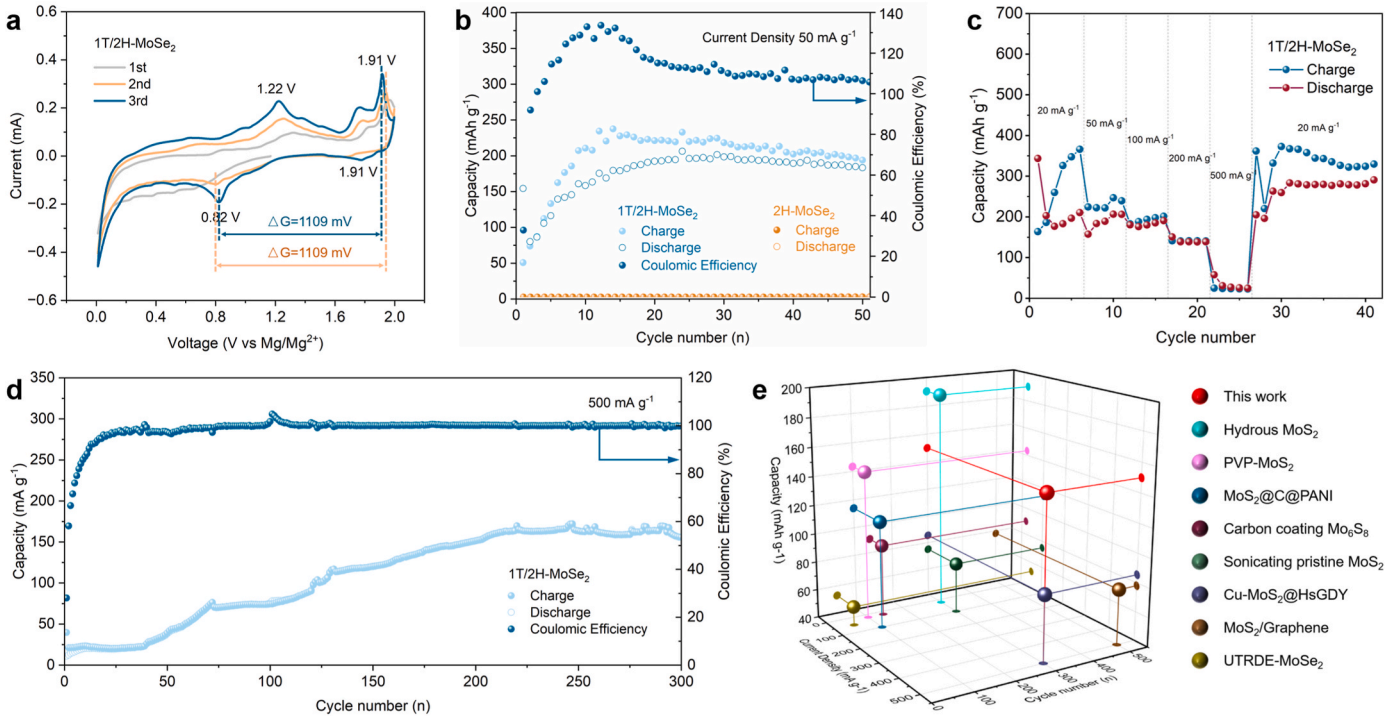

Fig. 2. a. CV curves of 1T/2H-$MoSe_2$ at 0.1 mV s^{-1}. b. Cycling performance of 1T/2H-$MoSe_2$ and 2H-$MoSe_2$ at the current density of 50 mA g^{-1}. c. Rate capabilities of 1T/2H-$MoSe_2$. d. Long-term cycling stability of 1T/2H-$MoSe_2$ at 50 mA g^{-1}. e. Comparison of cycling performances of 1T/2H-$MoSe_2$ with reported Mo-based cathode materials.

Fan et al. on SEI evolution in homologous APC electrolytes, the SEI in APC-based MIBs undergoes a three-stage dynamic process. In the initial formation stage, the high charge density of Mg^{2+} drives strong interactions with APC electrolyte components (e.g., THF solvent and Cl-containing species), triggering electrolyte decomposition and deposition of a primary SEI layer consisting of inorganic phases ($MgCl_2$, trace MgO) and organic phases (THF decomposition derivatives) on the electrode surface [30]. This process consumes partial active Mg^{2+} and electrolyte, directly contributing to the low initial Coulombic efficiency observed in this work. In the dissolution and purification stage, The trace H_2O and unstable chloride species in the primary SEI are gradually removed via electrochemical dissolution, leading to a denser and more homogeneous SEI structure [31]. This is consistent with the gradual increase of Coulombic efficiency from 31 % to over 90 % in our cycling tests (Fig. 2b). In the final stabilization stage, a mature SEI layer with inorganic phase dominance ($MgCl_2$-rich) is formed. This stabilized SEI effectively inhibits continuous electrolyte decomposition and reduces interfacial resistance, as evidenced by the electrochemical impedance spectroscopy (EIS) results in our work (Fig. 4a–b). Secondly, during the solvothermal synthesis, trace unreacted N_2H_4 remains in the 1T/2H-$MoSe_2$ nanoflowers. These residual amines react with Cl^- in the APC electrolyte to generate unstable intermediates (e.g., NH_4Cl), consuming active Mg^{2+} and reducing initial Coulombic efficiency. It is important to note that irreversible capture of Mg^{2+} could also result in this outcome [32]. During the initial magnesiation process, Mg^{2+} tend to form strong ionic covalent bonds with surface selenium atoms, resulting in the partial irreversible adsorption of Mg^{2+} at the defect sites [33]. In the ensuing activation process, the coulomb efficiency exceeds 100 %, a phenomenon attributable to the gradual activation of hidden active sites (e.g., heterophase junction structure) and the inhibition of self-discharge by the mature SEI film [17,18,34]. After 50 cycles, the discharge capacity of 1T/2H-$MoSe_2$ is found to be 183.37 mAh g^{-1}, and the Coulombic efficiency is close to 100 %. In contrast, the capacity of 2H-$MoSe_2$ is less than 50 mAh g^{-1} after 50 cycles, which is in accordance with the CV measurement. The enhanced performance exhibited by 1T/2H-$MoSe_2$ can be attributed to the presence of heterophase junction and its distinctive charge coupling.

In order to distinguish the independent effects of morphological regulation and heterophase construction on the Mg-storage performance of $MoSe_2$, this study compared the Mg-storage performance and mechanisms of 2H-$MoSe_2$ with different morphologies. Furthermore, it was revealed that the 1T/2H heterophase enhances performance. A thorough literature comparison further corroborates the critical role of heterophase construction in optimizing the Mg-storage performance of $MoSe_2$. For instance, the commercially 2H-$MoSe_2$ exhibits a limited capacity for Mg^{2+} adsorption, attributable to its low specific surface area. Its inherent interlayer structure imposes a high Mg^{2+} diffusion barrier, resulting in a capacity decline below 50 mAh g^{-1} after 50 cycles at 50 mA g^{-1}. Yang et al. prepared ultra-thin 2H-$MoSe_2$ nanosheet (with abundant atomic defects and exposed edge surfaces) via hydrothermal-hydrogen treatment. However, its initial discharge/charge capacities are only 84.8/48.3 mAh g^{-1}, and the subsequent reversible capacity stabilizes at approximately 40 mAh g^{-1}, as its performance is constrained by the semiconducting property of the single 2H phase [35]. Fan et al. constructed amorphous carbon-coated flake-like 2H-$MoSe_2$ nanoflowers, which exhibit a capacity decrease from 110 mAh g^{-1} to 89 mAh g^{-1} over 100 cycles (from the 3rd to the 100th cycle). Although this performance is superior to that of the commercial sample, it is still limited by the intrinsic kinetics of the pure 2H phase [36]. Gao et al. synthesized high-crystalline agglomerated thick-flake 2H-$MoSe_2$ via 300 °C heat treatment under an Ar/H_2 atmosphere, achieving the optimal performance among pure 2H-$MoSe_2$ samples. This material delivered a capacity of 173.8 mAh g^{-1} after 200 cycles at 0.5 A g^{-1}. The balanced structural stability and ion diffusion efficiency enabled by its high crystallinity and moderate agglomeration were key factors in this performance [22]. The aforementioned results indicate that the Mg-storage performance of pure 2H-$MoSe_2$ follows the order of agglomerated thick flakes, nanoflowers, ultra-thin nanosheets, commercial lamellae with respect to morphology. Remarkably, the 1T/2H-$MoSe_2$ heterophase (in nanoflower morphology) achieves a

breakthrough improvement in performance. The capacity and rate capability are enhanced by approximately 106 % compared with 2H-$MoSe_2$ nanoflowers and by approximately 358 % compared with ultra-thin 2H-$MoSe_2$ nanosheets. This enhancement is attributed to the metallic conductivity of the 1T phase and the charge coupling effect at the heterophasic interface. In contrast, these phenomena are absent in single-phase 2H-$MoSe_2$.

To further understand the magnesium storage performance of 1T/2H-$MoSe_2$, the rate capability was investigated, and the results are displayed in Fig. 2c. The discharge capabilities were evaluated to be 210.35, 205.96, 190.65, 138.46 and 24.73 mAh g^{-1} at 20, 50, 100, 200, and 500 mA g^{-1}, respectively. Theoretically, the specific capacity of 1T/2H-$MoSe_2$ is 222.85 mAh g^{-1}, which is marginally higher than the maximum experimentally measured capacity (210.35 mAh g^{-1} at a current density of 20 mA g^{-1}; see Fig. 2c). A direct comparison between the theoretical and experimental specific capacities is provided in Table S1, with an observed active site utilization efficiency of approximately 94.4 %. The minor discrepancy (5.6 %) is attributable to four primary factors. Initially, the subject under investigation is the capacity consumption by solid electrolyte interphase (SEI) formation. The initial formation of the SEI film consumes partial Mg^{2+} and electrolyte components, resulting in a capacity loss. Secondly, the EDX analysis (see Fig. S2) reveals a decrease in the Mo:Se atomic ratio to 1:1.85 after cycling, which is lower than the theoretical ratio of 1:2. This reduction in the Mo:Se atomic ratio results in a decrease in the number of Mg^{2+} adsorption sites, leading to an additional capacity loss [37]. Furthermore, DFT calculations indicate that some inner-layer active sites of the 2H phase are inaccessible due to steric hindrance in the initial cycles and are only gradually activated under high-rate cycling conditions [38,39]. Finally, strong ion-covalent bonds form between Mg^{2+} and surface Se atoms, resulting in the irreversible adsorption of partial Mg^{2+} at defect sites. Conversely, for 2H-$MoSe_2$, its theoretical capacity (58.65 mAh g^{-1}) exhibits a substantial discrepancy from the experimentally measured capacity (<50 mAh g^{-1} after 50 cycles), yielding a utilization efficiency of 82.2 %. This relatively lower efficiency is primarily attributed to the thick-layered structure of 2H-$MoSe_2$, which restricts the diffusion of Mg^{2+} and thus limits the accessibility of active sites. It is noteworthy that when the current density is restored to 20 mA g^{-1}, the capacity rebounds to 290.79 mAh g^{-1} (higher than the initial theoretical capacity). This finding suggests that 1T/2H-$MoSe_2$ exhibits a high degree of adaptability to variations in current density. These observations can be attributed to the further activation of interlayer sites in the 1T/2H heterophase during high-rate cycling. Additionally, the prolonged cycle performance demonstrated at a current density of 500 mA g^{-1} (see Fig. 2d) suggests that 1T/2H-$MoSe_2$ exhibits exceptional stability. Subsequent to activation, an initial ion transport pathway is formed. The SEI film undergoes a gradual adjustment to a thin and dense stable structure, a process that necessitates multiple charge-discharge cycles [40]. At this juncture, the number of active sites reaches its zenith, and the discharge capacity stabilizes at 172.2 mAh g^{-1}. After undergoing 300 cycles, the capacity remains at 155.99 mAh g^{-1}, exhibiting a capacity retention rate of 90.6 %. The average capacity degradation rate is only 0.17 % per cycle, which is considerably lower than the degradation rates of most TMCs/seleides-based cathode materials. This low degradation rate may be attributed to the structural stability of the heterogeneous interface and the capacitive-dominated reaction, which avoids severe phase transitions. As can be seen in Fig. 2e, the magnesium storage capacity of 1T/2H-$MoSe_2$ at high current density is notably higher than that of other Mo-based materials reported [35,41–46]. The specific magnesium storage performance of Mo-based materials is compared in Table S2.

The level of polarization was evaluated by calculating the difference value between the charging and discharging voltage platform (△E) and the voltage difference of the main redox and reduction peak (△G). The results obtained indicated that 1T/2H-$MoSe_2$ exhibited a lower degree of polarization (Fig. 3a–c). A pronounced change in the morphology of the cathode material was detected by *ex*-SEM (Fig. 3d). Following cycling, 1T/2H-$MoSe_2$ with cluster nanoflower micromorphology converts to a layered stacking structure, and the lateral dimensions of the partially cycled lamellae significantly decrease, allowing better adaptation to the rapid (de)magnesiation [47]. This transformation facilitates the interface between the electrode and the electrolyte as well as

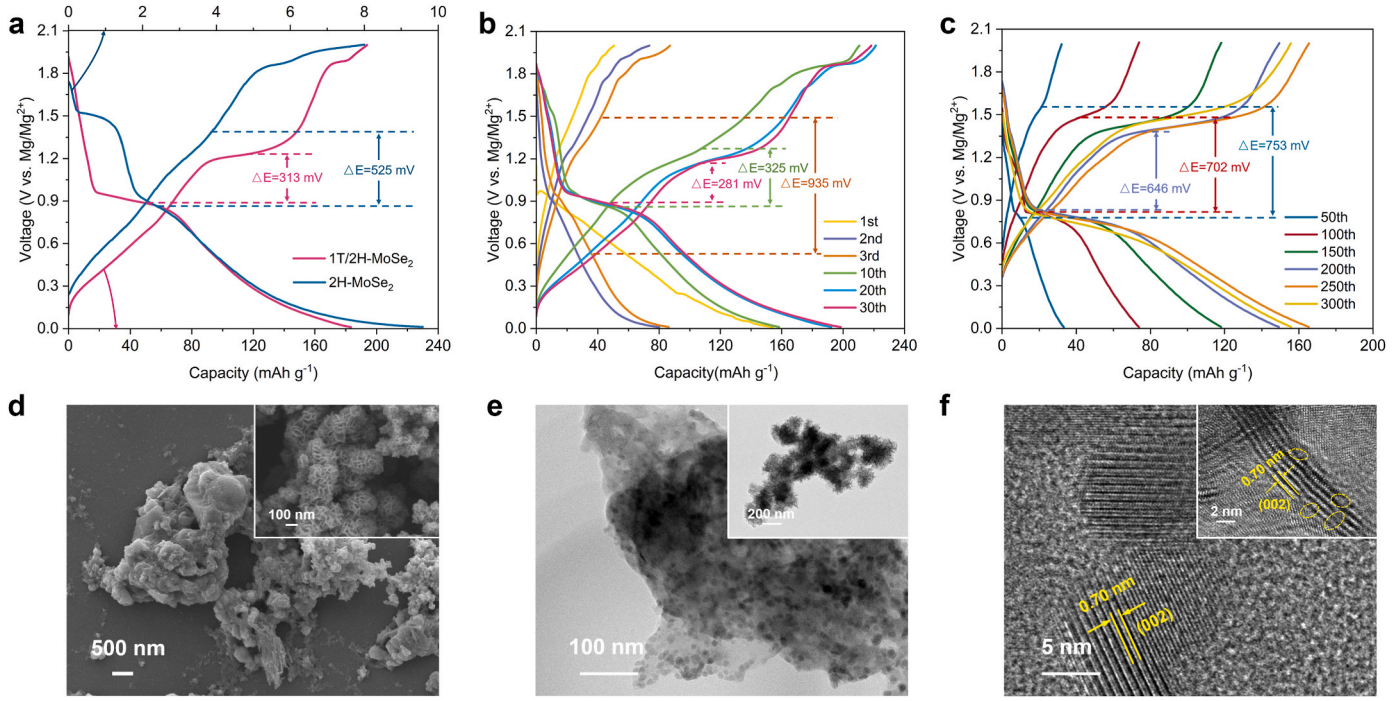

Fig. 3. a. Comparison of charge-discharge voltage profiles at 50 mA g^{-1} and calculated ΔE and ΔG values of 1T/2H-$MoSe_2$ and 2H-$MoSe_2$. The ΔE value of 1T/2H-$MoSe_2$ at b. 50 mA g^{-1} and c. 500 mA g^{-1}. d. SEM images, e. TEM images and f. HRTEM images of 1T/2H-$MoSe_2$ electrode at a current density of 500 mA g^{-1} after cycling (the inset figures are before cycling).

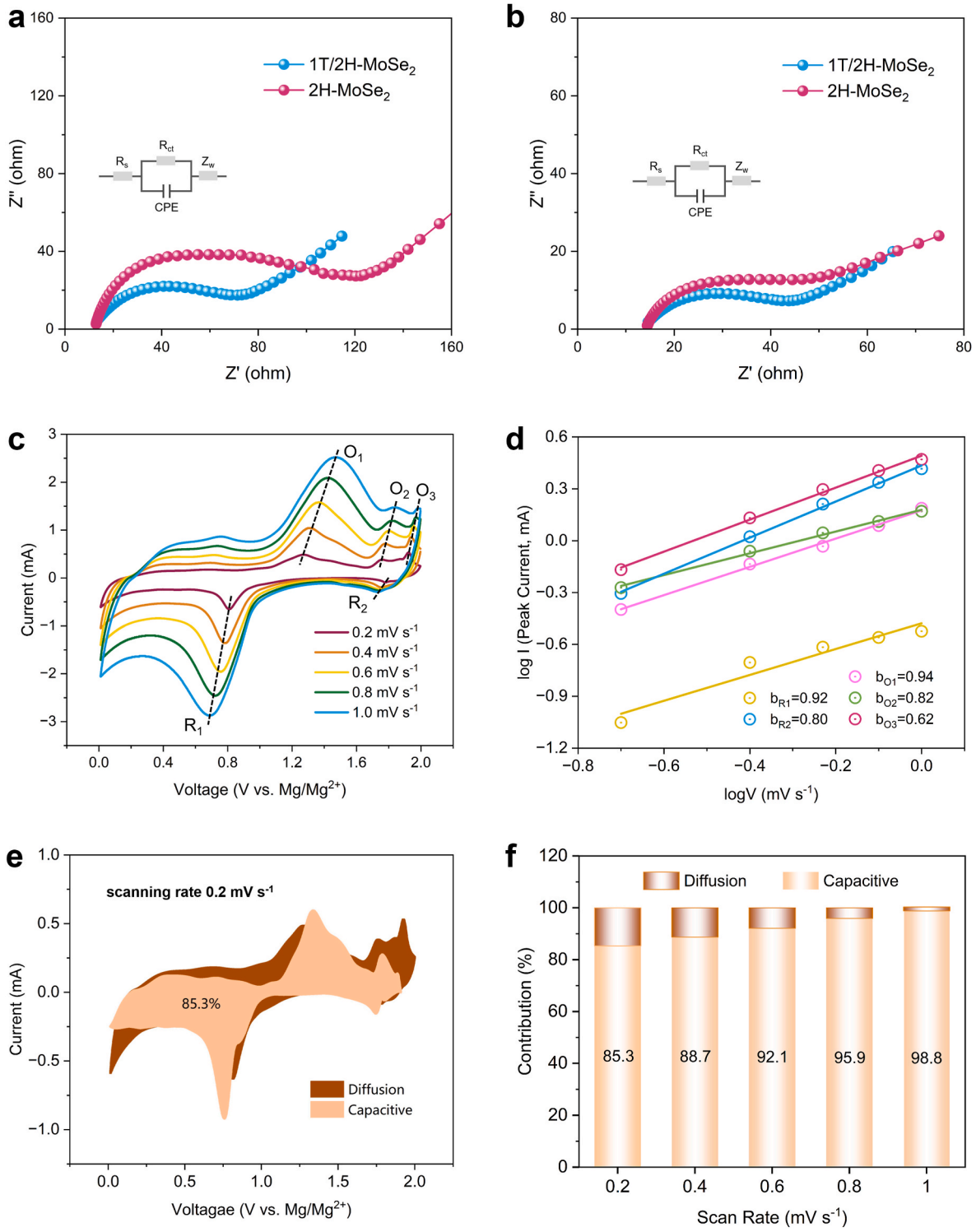

Fig. 4. a. EIS date of 1T/2H-$MoSe_2$ and 2H-$MoSe_2$ before cycling. b. EIS date of 1T/2H-$MoSe_2$ and 2H-$MoSe_2$ after cycling. c. CV curves at different scan rates from 0.2 to 1.0 mV s^{-1}, d. log(I) and log(V) plots at different oxidation and reduction peaks, e. capacitive contribution of 1T/2H-$MoSe_2$ at 0.2 mV s^{-1}, f. the diffusion controlled and capacitive capacities of 1T/2H-$MoSe_2$ at different scan rates.

the charge transfer behavior. Initially, the nanoflower-like morphology, characterized by abundant three-dimensional (3D) hierarchical branches and high specific surface area, provides numerous exposed active sites for Mg^{2+} storage. However, the loose and discrete nature of nanoflower may lead to uneven contact with the electrolyte, accompanied by localized concentration gradients of Mg^{2+} and increased interfacial resistance, as observed in previous studies on TMCs [48]. In this study, the transformation directly alleviated the volume expansion. The dense nanoflower clusters, which are subject to volume expansion during the Mg^{2+} insertion process, exhibit a layered stacking structure that provides ample space for buffering the expansion, thereby mitigating structural collapse. The loose layered structure of the material in question has been shown to facilitate the penetration of electrolytes and the access of Mg^{2+} to their active sites. In contrast, the formation of

layered stacked structures during charge/discharge processes induces a more ordered arrangement of crystallites, which significantly optimizes the interfacial wettability and contact uniformity between the electrode and electrolyte. This improved contact facilitates the establishment of continuous ion transport channels across the interface, as demonstrated by Shi et al. in their investigation on layered metal oxides for MIBs [49]. Moreover, the layered stacking effectively reduces the tortuosity of electron conduction paths within the electrode. The close packing of layers enhances the intergrain electronic conductivity, while the well-defined interlayer spacing provides favorable pathways for Mg^{2+} diffusion [5]. Consequently, the charge (electron and Mg^{2+}) transport kinetics across the interface is accelerated, as evidenced by the decreased Rct in EIS measurements. Simultaneously, this morphological evolution lowers the activation energy barrier for Mg^{2+} adsorption/-desorption and intercalation/deintercalation processes, as confirmed by CV with reduced peak potential separations, which aligns with the theoretical calculations of Mg^{2+} migration energy in layered structures. Collectively, the transformation from nanoflower-like to layered stacked structures not only strengthens the electrode-electrolyte interaction but also synergistically promotes both electron and ion transport, thereby contributing to enhanced rate capability, improved cycling stability, and increased Coulombic efficiency of MIBs. As illustrated in the TEM image (Fig. 3e), the presence of some particles on the lamella is evident, which were not observed in the unrecycled material. Furthermore, the HRTEM image of recycled 1T/2H-$MoSe_2$ (Fig. 3f) demonstrates that repeated charging and discharging does not enhance the lattice spacing of the electrode material [50]. The analysis suggests that the change in polarization degree is not due to an increase in lattice spacing, but rather to a change in morphology.

The CV measurements, conducted at scanning speeds ranging from 0.2 to 1.0 mV s^{-1}, were undertaken to investigate the electrochemical reaction of 1T/2H-$MoSe_2$ and were analysed by Eqs. S1 and S2. The b values of the redox peaks range from 0.92 to 0.80 (Fig. 4d), thereby confirming that the cathode reaction is dominated by a capacitive process. This mechanism is particularly well-suited for Mg^{2+} storage, as evidenced by its ability to facilitate the rapid movement of Mg^{2+}. Mg^{2+} exhibits robust Coulombic interactions with the host lattice, thereby establishing a substantial diffusion barrier in diffusion-controlled processes [51]. The capacitive process is contingent upon the surface/near-surface adsorption of Mg^{2+}, a strategy that circumvents the necessity for long-range solid-state diffusion, thereby reducing the energy barrier. Moreover, capacitive Mg^{2+} storage is predicated on weak physical/chemical adsorption, as opposed to irreversible phase transitions. This approach, consequently, engenders enhanced cycling stability [52]. The 1T/2H heterophase junction has been shown to promote the capacitive process through a combination of synergistic effects. The 1T-phase has been demonstrated to facilitate expeditious electron transfer pathways, thereby ensuring a rapid supply of charge to Mg^{2+} adsorption sites and enhancing the capacitive reaction kinetics [47]. In contrast, the 2H-phase contains a high concentration of Se atoms with unpaired electrons, which form ion-covalent bonds with Mg^{2+}. This process facilitates pseudocapacitive storage. As demonstrated in Fig. 5c–d, DFT calculations reveal that the heterophase junction induces electron enrichment at the interface, thereby increasing the density of Mg^{2+} adsorption sites in comparison to single-phase $MoSe_2$. The interface coupling phenomenon has been shown to have a direct impact on the reduction of Rct, thereby enhancing the capacitive behavior of the system. Additionally, the b values of the oxidation peaks are approximately 0.62 and 0.94, indicating that on the anode side, the processes are governed by both diffusion-controlled and capacitive processes (see Fig. 4c–d). This is due to the Mg^{2+} intercalating into the Mg foil anode, involving both surface adsorption and bulk diffusion. Furthermore, it has been demonstrated that the capacitive effect increases with the increase of scan rate from 0.2 to 1.0 mV s^{-1} (Fig. 4e and Fig. S7), and that the proportion attains 98.8 % when the scan rate is 1.0 mV s^{-1} (Fig. 4f).

In order to verify the improved charge transfer kinetics characteristics of 1T/2H-$MoSe_2$, EIS measurements were conducted (see Fig. 4a–b). The results of the equivalent circuit fitting indicated that the Rct of 1T/2H-$MoSe_2$ was significantly lower than that of 2H-$MoSe_2$. This was attributed to the metallic conductivity of the 1T phase and the interfacial coupling of the heterogeneous interface, which accelerated the electron transfer between the electrode and the electrolyte. Following 300 cycles at a current density of 500 mA g^{-1}, the Rct of 1T/2H-$MoSe_2$ exhibited an increase, suggesting the presence of a stable charge transfer path. This can be attributed to the layered stacking morphology (Fig. 3d), which facilitates the maintenance of contact between the electrode and the electrolyte. Conversely, following cycling, there was a pronounced increase in the Rct of 2H-$MoSe_2$, attributable to agglomeration and an augmentation in SEI thickness. These EIS results directly corroborated the theoretical prediction of enhanced charge transfer kinetics in 1T/2H-$MoSe_2$ [22].

As demonstrated in Fig. 5a-b, following the intercalation of Mg^{2+} into 2H-$MoSe_2$, the electron redistribution primarily occurs between

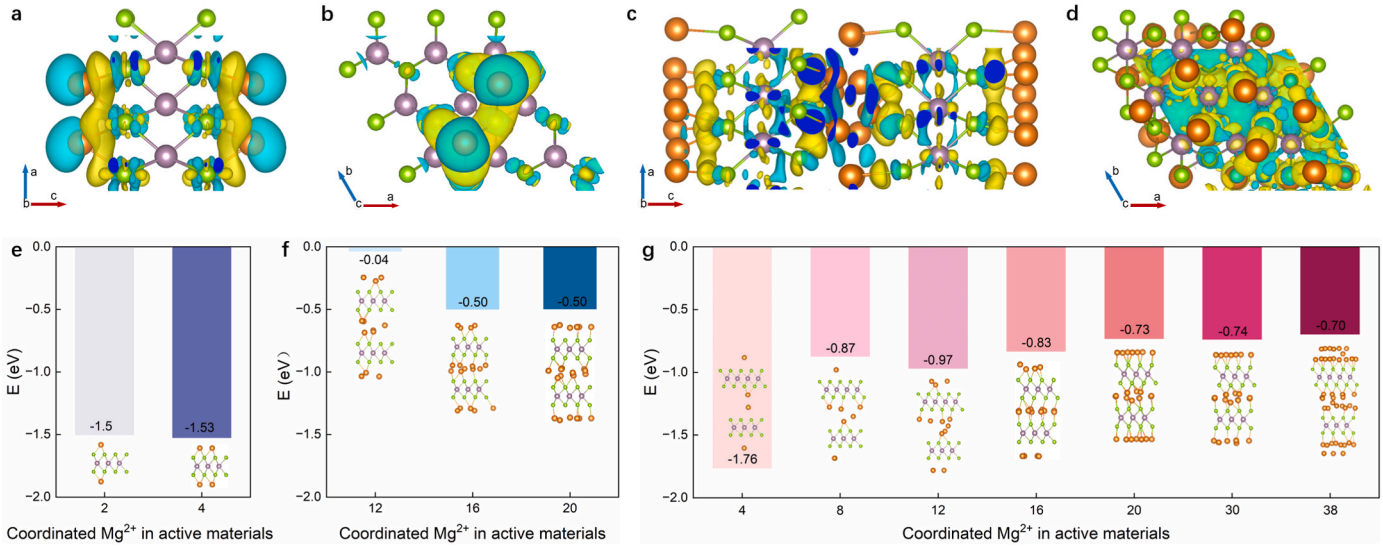

Fig. 5. Charge density difference of 2H-$MoSe_2$-Mg, (a) side view and (b) top view. Charge density difference of 1T/2H-$MoSe_2$-Mg, side view(c) and top view (d). The adsorption energies of Mg^{2+} of different concentrations on (e) 2H-$MoSe_2$, (f) 2H/2H-$MoSe_2$ and (g) 1T/2H-$MoSe_2$.

Mg^{2+} and Se, thereby unveiling a substantial ion-covalent mixing interaction with the matrix material. However, the overall charge transfer range is limited, and the charge enrichment and depletion are more concentrated in the area adjacent to Mg^{2+}. In contrast, the charge density difference of the 1T/2H-$MoSe_2$ presents more complex (Fig. 5c-d). It is evident that electron enrichment and loss occur in the Mg^{2+} vicinity. Additionally, stronger charge coupling characteristics are manifest in the heterophase junction interface, interlayer, and surface regions. This mechanism is consistent with the previous analysis of Mg^{2+} storage performance. The findings demonstrate that the charge transfer process in the 1T/2H-$MoSe_2$ system overcomes the restriction imposed by Mg^{2+} adsorption sites, thereby generating a synergistic enhancement effect in the interface region [10]. This effect can significantly promote the adsorption, migration, and deintercalation processes of Mg^{2+} [5,53].

The optimized structure during the Mg^{2+} intercalation process is illustrated in Fig. 5e-f & S8. The Gibbs free energy changes (ΔG) of the 2H-$MoSe_2$, 2H/2H-$MoSe_2$, and 1T/2H-$MoSe_2$ heterophase junctions after combining with Mg^{2+} are still negative, suggesting that all three materials can spontaneously accommodate the storage of multiple Mg^{2+} theoretically. The heterophase of 1T/2H-$MoSe_2$ demonstrates a lowest kinetic energy barrier for Mg^{2+} migration. The b-value corresponding to the redox peaks of 1T/2H-$MoSe_2$ ranges from 0.80 to 0.94 via CV scan rate dependence analysis, and the capacitive contribution reaches 98.8 % at a scan rate of 1.0 mV s^{-1}. This finding suggests that the Mg^{2+} storage behavior is predominantly influenced by surface/near-surface pseudocapacitive processes, thereby circumventing the high barrier issue associated with long-range diffusion. DFT calculations reveal a significant electron accumulation at the heterophase interface, which can effectively weaken the Coulomb repulsion between Mg^{2+} and the host lattice. Following the cycling process, the initial nanoflower-like morphology undergoes a transformation into a layered stacking structure, thereby further reducing the Mg^{2+} diffusion path. Concurrently, results of EIS indicate a substantial decrease in Rct. It has been established through previous studies that there is a correlation between the phase structure of Mo-based TMCs and ion migration barriers. For instance, the Mg^{2+} diffusion barrier of semimetallic Hae-MoS_2 monolayers is 0.30 eV, which is lower than that of semiconducting phase H-MoS_2 and Hae-MoS_2 bilayers [54]. Analogous to this, it can be inferred that the metallic 1T phase in 1T/2H-$MoSe_2$ provides a rapid transport channel for Mg^{2+}, while the heterophase interface further optimizes the migration barrier [17,55].

However, the mechanisms of Mg^{2+} intercalating in each matrix and the saturation capacity are different. As demonstrated in Fig. S8, the Mg^{2+} in 2H-$MoSe_2$ is predominantly deposited on the surface through ion-covalent bond interactions. It has been observed that, upon attaining a Mg^{2+} concentration of 0.56, the system exhibits structural instability. The △G of its 2H-$MoSe_2$-$Mg_{0.56}$ configuration is −1.53 eV, corresponding to the storage of Mg^{2+} at the surface Se atomic sites. Conversely, in the 1T/2H-$MoSe_2$ and 2H/2H-$MoSe_2$, the deposition of Mg^{2+} can occur at the interface, interlayer, and surface regions of the heterophase junctions. Among them, 1T/2H-$MoSe_2$ exhibits a higher saturated adsorption capacity and attains adsorption saturation when the Mg^{2+} concentration reaches 4.22. Regrettably, further adsorption leads to structural disintegration, as observed in 2H-$MoSe_2$-$Mg_{0.56}$. The aforementioned results indicate that the 1T/2H heterophase junction benefits from a stronger interfacial electronic coupling effect, which significantly improves the utilization rate of active sites [56]. Furthermore, the theoretical calculated saturated adsorption capacity is consistent with the experimental results, thereby providing additional confirmation that the 1T/2H phase can optimize storage performance by enhancing the charge exchange and transfer process between Mg^{2+} and the material.

4. Conclusions

To summarize, the $MoSe_2$ with phase of 1T and 2H was prepared via a straightforward solvothermal method. 1T/2H-$MoSe_2$ exhibited an exceptional capacity of 183.37 mAh g^{-1} at 50 mA g^{-1} over 50 cycles, and demonstrated an optimal capacity of 155.99 mAh g^{-1} at 500 mA g^{-1} over 300 cycles. As the cycle progresses, the morphology of the cathode material changes, promoting full contact between the electrode material and the electrolyte, thereby improving the current transfer speed and reducing the degree of activation. Experimental results and DFT calculations reveal the contribution of heterophase junction to cycling stability and capacity. Heterophase junctions enhance ionic covalent bonds and interfacial electronic coupling effects between Mg^{2+} and surface Se atoms, reducing the energy barrier for Mg^{2+} insertion and increasing the storage capacity of magnesium. This study demonstrates the impact of heterophase junction on the electrochemical performance of $MoSe_2$ for MIBs.

CRediT authorship contribution statement

Wei Yu: Writing – review & editing, Writing – original draft, Visualization, Validation, Supervision, Software, Resources, Project administration, Methodology, Investigation, Formal analysis, Data curation, Conceptualization. **Yue Yang:** Visualization, Validation, Supervision, Software, Investigation, Formal analysis, Data curation, Conceptualization. **Liuyu Song:** Writing – original draft, Visualization, Validation, Software, Investigation, Data curation, Conceptualization. **Wenhao Zhou:** Visualization, Validation, Software. **Xi Chen:** Software, Resources, Formal analysis, Data curation, Conceptualization. **Lin zhu:** Software. **Miao Xu:** Resources, Methodology, Investigation. **Fan Mo:** Writing – review & editing, Software, Resources, Project administration, Methodology, Investigation, Data curation, Conceptualization. **Haibo Li:** Writing – review & editing, Resources, Methodology, Investigation, Funding acquisition.

Declaration of competing interest

The authors declare no conflicts of interest.

Acknowledgments

This work was supported by the Key Technologies Research and Development Program [Grant Numbers 2024YFC2909605], Project of Shenyang Science and Technology Program [Grant Numbers 24-216-2-07] and Fundamental Research Funds for the Cornell University [Grant Numbers N25BSS006], [NO. N25ZLE003] & [NO. N25XQD083].

Appendix A. Supplementary data

Supplementary data to this article can be found online at https://doi.org/10.1016/j.jpowsour.2025.238971.

Data availability

Data will be made available on request.

References

[1] J. Rahmatinejad, X. Liu, B. Raisi, Z. Ye, Synergistic cathode design for high-performance dual-salt Magnesium/lithium-ion batteries using 2D/2D 1T/2H-MoS_2@$Ti_3C_2T_x$ MXene nanocomposite, Small 20 (36) (2024) 2401391.
[2] H. Lv, O. Fang, S. Ren, G. Xu, S. Ding, Z. Li, Cationic/anionic vacancies constructed in WSe_2 toward enhanced performance of rechargeable magnesium batteries, ACS Sustain. Chem. Eng. 12 (37) (2024) 13929–13936.
[3] J. Wang, G. Yang, T. Ghosh, Y. Bai, C.Y.J. Lim, L. Zhang, D.H.L. Seng, W.P. Goh, Z. Xing, Z. Liu, Z.W. Seh, Hierarchical FeS_2 cathode with suppressed shuttle effect for high performance magnesium-ion batteries, Nano Energy 119 (2024) 109082.
[4] X. Qu, G. Li, F. Wang, Y. Zhang, T. Gao, Y. Luo, Y. Song, F. Fang, D. Sun, F. Wang, Y. Liu, In-situ electrochemical activation accelerates the magnesium-ion storage, Nat. Commun. 16 (1) (2025) 1310.

[5] S. Huo, H. Qu, F. Meng, Z. Zhang, Z. Yang, S. Zhang, X. Hu, E. Wu, Negative differential resistance with ultralow peak-to-valley voltage difference in Td-WTe_2/2H-MoS_2 heterostructure, Nano Lett. 24 (38) (2024) 11937–11943.

[6] X. Chen, A. Zhang, H. Zou, L. Li, Q. Zhu, W. Zhang, Defect engineering modulated $MoSe_2$ cathode achieves highly effective photo-responsive zinc ion battery, Energy Storage Mater. 70 (2024) 103457.

[7] J. Yuan, P. Wang, N. Song, Y. Wang, J. Ma, S. Xiong, X. Li, J. Feng, B. Xi, Alloying strategy regulating size and electronic structure of $Mo_{0.25}Nb_{0.75}Se_2$ to achieve high-performance lithium-sulfur batteries, Angew. Chem. Int. Ed. 64 (9) (2024) e202420866.

[8] Y. Chao, S. Jia, J. Li, G. Chen, L. Liu, F. Tang, J. Zhu, C. Wang, X. Cui, A dual heterostructure enables the stabilization of 1T-rich $MoSe_2$ for enhanced storage of sodium ions, Chem. Sci. 15 (28) (2024) 11134–11144.

[9] Z. Xie, S. Yu, X. Ma, K. Li, L. Ding, W. Wang, D.A. Cullen, H.M. Meyer III, H. Yu, J. Tong, Z. Wu, F.Y. Zhang, MoS_2 nanosheet integrated electrodes with engineered 1T-2H phases and defects for efficient hydrogen production in practical PEM electrolysis, Appl. Catal. B Environ. Energy 313 (2022) 121458.

[10] C. Li, X. Chen, Z. Zhang, X. Wu, T. Yu, R. Bie, D. Yang, Y. Yao, Z. Wang, L. Sun, Charge-selective 2D heterointerface-driven multifunctional floating gate memory for in situ sensing-memory-computing, Nano Lett. 24 (47) (2024) 15025–15034.

[11] G. Kresse, J. Furthmuller, Efficient iterative schemes for ab initio total-energy calculations using a plane-wave basis set, Phys. Rev. B 54 (16) (1996) 11169–11186.

[12] G. Kresse, D. Joubert, From ultrasoft pseudopotentials to the projector augmented-wave method, Phys. Rev. B 59 (3) (1999) 1758–1775.

[13] J.P. Perdew, K. Burke, M. Ernzerhof, Generalized gradient approximation made simple, Phys. Rev. Lett. 77 (18) (1996) 3865–3868.

[14] S. Grimme, Semiempirical GGA-type density functional constructed with a long-range dispersion correction, J. Comput. Chem. 27 (15) (2006) 1787–1799.

[15] T. Hong, Q. Zhou, Y. Liu, Y. Ji, S. Tan, W. Zhou, Z. Cai, Preparation of DNA nanoflower-modified capillary silica monoliths for chiral separation, Microchim. Acta 191 (10) (2024) 584.

[16] Y. Zhang, L. Zhang, B. Zhou, H. Cheng, Q. Zhang, B. Zhang, Hierarchical 2H/1T-$MoSe_2$@graphene on cotton fabric for multifunctional and flexible microwave absorption, Carbon 205 (2023) 562–572.

[17] L. Liu, B. Li, J. Wang, H. Du, Z. Du, W. Ai, Molecular intercalation enables phase transition of $MoSe_2$ for durable Na-Ion storage, Small 20 (24) (2024) 2309647.

[18] Z. Li, J. Yan, Q. Li, A. Xu, J. Sun, Y. Wang, X. Zhang, X. Sun, F. Jiang, Y. Zhou, Te doped 1T/2H-$MoSe_2$ nanosheets with rich defects as advanced anode materials for high-rate sodium ion half/full batteries, Inorg. Chem. Front. 11 (7) (2024) 2017–2028.

[19] F. Niu, Z. Bai, Y. Mao, S. Zhang, H. Yan, X. Xu, J. Chen, N. Wang, Rational design of MWCNTs@amorphous carbon@MoS_2: towards high performance cathode for aqueous zinc-ion batteries, Chem. Eng. J. 453 (2023) 139933.

[20] K. Xu, Y.H. Li, X. Wang, Y.P. Cao, S.T. Wang, L. Cao, Q.T. Zhang, Z.-F. Wang, J. Yang, Unlocking the structure and anion synergistic modulation of $MoSe_2$ anode for ultra-stable and high-rate sodium-ion storage, Rare Met. 44 (3) (2024) 1661–1673.

[21] Y. Liang, H. Dong, D. Aurbach, Y. Yao, Current status and future directions of multivalent metal-ion batteries, Nat. Energy 5 (9) (2020) 646–656.

[22] S. Gao, Z. Yang, Y. Hao, A. Xu, J. Yan, Z. Li, F. Jiang, Y. Wang, K. Zhang, Y. Zhou, Low-crystalline 1T/2H-$MoSe_2$ heterostructure as the high-rate and ultra-long-lifespan cathode materials for magnesium ion batteries, J. Energy Storage 101 (2024) 113890.

[23] D. Tao, Y. Tang, H. Gui, F. Xu, Facile fabrication of high-power Molybdenum diselenide cathode for rechargeable magnesium batteries, ACS Sustain. Chem. Eng. 12 (27) (2024) 10269–10275.

[24] Y. Cao, Y. Zhu, C. Du, X. Yang, T. Xia, X. Ma, C. Cao, Anionic Te-Substitution boosting the reversible redox in CuS nanosheet cathodes for magnesium storage, ACS Nano 16 (1) (2022) 1578–1588.

[25] Y. Xu, Y. Fo, H. Lv, X. Cui, G. Liu, X. Zhou, L. Jiang, Anderson-type polyoxometalate-assisted synthesis of defect-rich doped 1T/2H-$MoSe_2$ nanosheets for efficient seawater splitting and Mg/Seawater batteries, ACS Appl. Mater. Interfaces 14 (8) (2022) 10246–10256.

[26] C. Du, W. Younas, Z. Wang, X. Yang, E. Meng, L. Wang, J. Huang, X. Ma, Y. Zhu, C. Cao, Constructing sheet-assembled hollow CuSe nanocubes to boost the rate capability of rechargeable magnesium batteries, J. Mater. Chem. A 9 (6) (2021) 3648–3656.

[27] S. Ding, Z. Li, X. Dai, C. Sun, A. Meng, Mo-doped VS_4 with interlayer-expanded and engineering sulfur vacancies as cathode for advanced magnesium storage, Chem. Eng. J. 417 (2021) 129328.

[28] W. Yu, K.Y. Lin, D.T. Boyle, M.T. Tang, Y. Cui, Y. Chen, Z. Yu, R. Xu, Y. Lin, G. Feng, Z. Huang, L. Michalek, W. Li, S.J. Harris, J.C. Jiang, F. Abild-Pedersen, J. Qin, Y. Cui, Z. Bao, Electrochemical formation of bis(fluorosulfonyl)imide-derived solid-electrolyte interphase at Li-metal potential, Nat. Chem. 17 (2) (2025) 246–255.

[29] K. Zhang, Y. Ji, Q. Wu, S.A. Nabavizadeh, Y. Qi, L.Q. Chen, Simulating solid electrolyte interphase formation spanning 10^8 time scales with an atomically informed phase-field model, Energy Environ. Sci. 18 (15) (2025) 7541–7554.

[30] F. Wang, H. Hua, Y. Zhuang, J. Wu, J. Zeng, J. Zhao, A Li/Mg double-salt strategy based on amine solvent achieves bulk phase-interface-electrode multi-scale optimization for Mg metal batteries, Adv. Funct. Mater. 35 (4) (2025) 2414181.

[31] S. Fan, S. Cora, N. Sa, Evolution of the dynamic solid electrolyte interphase in Mg electrolytes for rechargeable Mg-Ion batteries, ACS Appl. Mater. Interfaces 14 (41) (2022) 46635–46645.

[32] L. Yang, A. Du, Z. Lv, Z. Zhang, G. Li, Emerging amine-assisted electrolytes for rechargeable magnesium metal batteries: current understanding and future direction, Chem. Eng. J. 506 (2025) 160376.

[33] Q. Kong, L. Cui, X. Liao, R. Yu, Y. Jiang, J. Wang, W. Zhang, Y. Wang, L. Zhang, Q. An, Bimetallic selenide $CuFeSe_2$ as Mg-Storage material for rechargeable magnesium batteries, Batt. Supercaps 7 (6) (2024) 2400055.

[34] R. Zhou, H. Wang, J. Chang, C. Yu, H. Dai, Q. Chen, J. Zhou, H. Yu, G. Sun, W. Huang, Ammonium intercalation induced expanded 1T-Rich molybdenum diselenides for improved lithium ion storage, ACS Appl. Mater. Interfaces 13 (15) (2021) 17459–17466.

[35] J. Yang, J. Wang, L. Zhu, X. Wang, X. Dong, W. Zeng, J. Wang, F. Pan, Enhancing Mg^{2+} and Mg^{2+}/Li^+ storage by introducing active defect sites and edge surfaces in $MoSe_2$, Chemelectrochem 8 (22) (2021) 4252–4260.

[36] J.J. Fan, S.Y. Shen, Y. Chen, L.N. Wu, J. Peng, X.X. Peng, C.G. Shi, L. Huang, W. F. Lin, S.G. Sun, A rechargeable Mg^{2+}/Li^+ hybrid battery based on sheet-like $MoSe_2$/C nanocomposites cathode, Electrochem. Commun. 90 (2018) 16–20.

[37] Z. Li, I. Sami, J. Yang, J. Li, R.V. Kumar, M. Chhowalla, Lithiated metallic molybdenum disulfide nanosheets for high-performance lithium-sulfur batteries, Nat. Energy 8 (1) (2023) 84–93.

[38] D. Zhu, Q. Dai, X. Zhang, J. Yi, Y. Yang, Synergistic nitrogen-doping and carbon-coating in N-$MoSe_2$/C nanoflowers enable ultra-high discharge capacity for Li-CO_2 batteries, J. Mater. Chem. A 13 (30) (2025) 24532–24541.

[39] Y. Shen, K. Xu, Z. Zhao-Karger, X. Zhao, Tailoring loose Mg^{2+} solvation structure by steric and competitive solvent coordination for fast-charging magnesium batteries, Energy Environ. Mater. 0 (2025) e70124.

[40] Z. Fan, W. Zhao, S. Shi, M. Zhou, J. Li, Y. Liu, Z. Pan, X. Yang, Regulating electric double layer via self-assembled monolayer for stable solid/electrolyte interphase on Mg metal anode, Angew. Chem. Int. Ed. 64 (4) (2025) e202416582.

[41] C. Wu, L. Zhang, G. Zhao, X. Yu, C. Liu, J. He, K. Sun, N. Zhang, Interlayer-expanded MoS_2 containing structural water with enhanced magnesium diffusion kinetics and durability, Chemelectrochem 8 (23) (2021) 4559–4563.

[42] W. Zhao, Y. Zhang, H. Li, K. Wang, K. Jiang, Large-scale fabricating carbon coating Chevrel phase in molten salts: implications for high-performance magnesium-ion battery cathode, J. Alloys Compd. 925 (2022) 166745.

[43] B. Li, Z. Li, H. Chen, X. Zhang, S. Wu, H. Xu, Y. Yao, Y. Li, X. Li, Z. Hu, R.M. Laine, J. Zou, K. Zhang, Li^+ additive accelerated structural transformation of MoS_2 cathodes for performance-enhancing rechargeable Mg^{2+} batteries, Mater. Today Energy 27 (2022) 101047.

[44] J. Liu, Y. Zhong, X. Li, T. Ying, T. Han, J. Li, A novel rose-with-thorn ternary MoS_2@carbon@polyaniline nanocomposite as a rechargeable magnesium battery cathode displaying stable capacity and low-temperature performance, Nanoscale Adv. 3 (19) (2021) 5576–5580.

[45] C. Wu, G. Zhao, X. Yu, C. Liu, P. Lyu, G. Maurin, S. Le, K. Sun, N. Zhang, MoS_2/graphene heterostructure with facilitated Mg-diffusion kinetics for high-performance rechargeable magnesium batteries, Chem. Eng. J. 412 (2021) 128736.

[46] C. Wu, G. Zhao, S. Gong, N. Zhang, K. Sun, PVP incorporated MoS_2 as a Mg ion host with enhanced capacity and durability, J. Mater. Chem. A 7 (9) (2019) 4426–4430.

[47] X.F. Ma, H.Y. Li, J. Tan, J. Wang, J. Diao, J. Yue, S. Tan, G. Huang, J. Wang, F. Pan, Anisotropy of V_3O_7 nanobelts enables ultralong cycling life of magnesium ion battery, J. Magnesium Alloys 13 (4) (2025) 1592–1601.

[48] N. Shi, X. Li, G. Liu, Y. Liang, C. Sun, X. An, B. Xi, S. Xiong, $MoSe_2/Bi_2Se_3$ heterostructure immobilized in N-Doped carbon nanosheets assembled flower-like microspheres for high-rate sodium storage, Small 21 (17) (2025) 2412304.

[49] R. Shi, S. Jiao, Z. Yang, Z. Bo, J. Jiao, Y. Zhao, Regulating interfacial wettability for fast mass transfer in rechargeable metal-based batteries, ACS Nano 19 (9) (2025) 8462–8508.

[50] L. Fang, H. Li, B.B. Xu, J. Ma, H. Pan, Q. He, T. Zheng, W. Ni, Y. Lin, Y. Li, Y. Cao, C. Sun, M. Yan, W. Sun, Y. Jiang, Latticed-confined conversion chemistry of battery electrode, Small 18 (48) (2022) 204912.

[51] Z. Fan, R. Li, X. Zhang, W. Zhao, Z. Pan, X. Yang, Defect engineering: can it mitigate strong coulomb effect of Mg^{2+} in cathode materials for rechargeable magnesium batteries? Nano-Micro Lett. 17 (1) (2025) 4.

[52] H. Ma, H. Chen, M. Wu, F. Chi, F. Liu, J. Bai, H. Cheng, C. Li, L. Qu, Maximization of spatial charge density: an approach to ultrahigh energy density of capacitive charge storage, Angew. Chem. Int. Ed. 59 (34) (2020) 14541–14549.

[53] H. Zheng, D. Ma, M. Pei, C. Lin, Y. Liu, S. Deng, R. Qiu, Y. Luo, W. Yan, J. Zhang, Heterojunction vacancies-promoted high sodium storage capacity and fast reaction kinetics of the anodes for ultra-high performance sodium-ion batteries, Adv. Funct. Mater. 35 (1) (2025) 2411651.

[54] J. Hu, W. Jin, Z. Tan, S. Wu, J. Tian, Y. Sun, C.C. Ding, Potential application of 2D haeckelite MoS_2 as an anode material for Mg ion batteries, Langmuir 40 (37) (2024) 19396–19403.

[55] F. Creazzo, Engineering of $MoSe_2$ and WSe_2 monolayers and heterostructures by DFT-molecular dynamics simulations, ACS Appl. Mater. Interfaces 17 (27) (2025) 39676–39693.

[56] X. Qi, Y. Zhu, Y. Xu, W. Chen, Z. Hu, L. Xi, Y. Xie, H. Hou, G. Zou, X. Ji, Phase engineering enables ultrahigh-capacity 1T/2H-MoS2 for advanced ammonium-ion storage, Energy Storage Mater. 75 (2025) 104063.